# IMPACT OF P-1 RADIATION MODEL ON SIMULATED FREE JET FLAME CHARACTERISTICS OF GASEOUS FUELS
## The CFD with PDF Approach

by

***Hassan F. ELATTAR[a,b*], Eckehard SPECHT[c], Bandar Awadh ALMOHAMMADI[d], Mohamed H. MOHAMED[e], and Hassanein A. REFAEY[d,f]***

[a] Department of Mechanical Engineering, Benha Faculty of Engineering,
Benha University, Benha, Egypt
[b] Department of Mechanical and Materials Engineering, Faculty of Engineering,
University of Jeddah, Asfan Road, Jeddah, Saudi Arabia
[c] Institute of Fluid Dynamics and Thermodynamics,
Otto-von-Guericke-University of Magdeburg, Magdeburg, Germany
[d] Department of Mechanical Engineering, College of Engineering at Yanbu,
Taibah University, Yanbu Al-Bahr, Saudi Arabia
[e] Mechanical Engineering Department, College of Engineering and Islamic Architecture,
Umm Al-Qura University, Makkah, Saudi Arabia
[f] Department of Mechanical Engineering,
Faculty of Engineering at Shoubra, Benha University, Cairo, Egypt

Original scientific paper
https://doi.org/10.2298/TSCI230109038E

*Simulation and analysis of a turbulent free jet flame erupting into still air are done using CFD. Using 2-D axisymmetric numerical modelling in ANSYS-FLUENT 14.5. Three distinct kinds of gaseous fuels are used: $CH_4$, CO, and biogas (50% $CH_4$ and 50% $CO_2$). The effects of thermal radiation modelling utilizing the P-1 radiation model on the behavior of a free jet flame are investigated, and the impacts of air temperature and fuel velocity on the flame length are also provided. The findings demonstrated that the radiation modelling did not affect the temperature distribution and flame length for CO and biogas (i.e., lower heating value fuels). Nevertheless, the air temperature and fuel kind considerably impact the flame behavior. While the fuel inlet velocity (i.e., burner power) does not affect the flame length. Additionally, free jet flame velocity and length numerical correlations considering radiation modelling are predicted and presented with allowable errors. A comparison with earlier experimental correlation proved successful, with a maximum error of ±9.4%.*

Key words: *CFD simulation, free jet flame, P-1 radiation model, non-premixed flame, flame length*

## Introduction

Flames are often used in turbulent jets in various practical combustion processes, such as crystallization, mixing, drying, precipitation, polymerization, and extraction. Some industrial processes were devised and developed to produce desired products. Using unbounded (free) and bounded jets for these processes is applicable because they are simple to implement, output highly turbulent flows, and have high mixing efficiencies. A jet that exits the nozzle due to a

* Corresponding author, e-mail: hassan.alattar@bhit.bu.edu.eg

pressure differential and is injected quickly into the medium without taking the impact of any solid boundaries into account is referred to as a free jet. The fluid dynamics behavior through the jet controls heats and mass transfer between free jets and between a jet and a surface (solid or liquid). The non-premixed free jet flames are widely used in useful applications, such as power plants [1], rocket engines [2], and gas turbines [3]. Because of their basic influence on combustion parameters, flame shape and dimensions, particularly flame length, are critical for jet flames. The flame length may easily describe several flame features, such as thermal radiation and pollutant emission. Furthermore, flame length and shape are required for the design and operation of combustion systems or gas burners, where the flame dimensions often define the combustion system dimensions. Due to the contact between the free shear layer and the jet, more sophisticated computational modelling methods are needed to capture the characteristics of turbulent compound flows accurately. Gaseous fuels are also used to generate energy, and their combustion properties during energy conversion have garnered study. The CFD has been used for years to create and improve chemical engineering equipment and processes. Experimental and numerical research on turbulent-free jets is substantial.

For a lifted flame, non-premixed $CH_4$ for turbulent free jet flame injected into still flowing gas, Mahmud *et al.* [4] examined and presented experimentally and numerically the in-flame observations, involving the gas temperature, oxygen, and concentration distributions of NO. This raised, non-premixed, turbulent free jet flame's combustion and NO features can now be more accurately visualized credits to experimental data collected directly from the flame. Concerning the most modern method of visualizing a flame, Lawn [5] highlighted the three most important ideas for regulating the height of the flames on fuel jets operating in co-flow air (experimental and computational review). In exchange for information from various investigations, the authors proposed new data for a Methane jet with flames created in a stream of co-flowing air that spreads outward. Houf *et al.* [6] completed an experimental and numerical analysis at Sandia National Laboratories to demonstrate and forecast the performance of inadvertent Hydrogen emissions. It was determined whether the calculated temperature profiles for turbulent free hydrogen jet flames at the laboratory size agreed with the experimental data. Jiang *et al.* [7] examined the non-premixed $C_3H_8$-air micro flame characteristics experimentally. The results demonstrated that ignited non-premixed $C_3H_8$-air could form a balanced flame depending on equivalence ratio and inlet velocity. Choi and Chung [8] conducted experiments on the impacts of starting temperature deviation on the steadiness characteristics of non-premixed turbulent flames in co-flow jets with $CH_4$ fuel diluted by $N_2$. Based on the results, the unburned fuel-air mixture's features significantly influence flame steadying in co-flow jets when the initial conditions are altered. The Oh and Noh [9] studied and published the characteristics of oxy-methane flames in a laboratory-scale slot burner under atmospheric circumstances (298 K and 1 bar). An increase in oxygen and fuel velocities results in a longer flame and greater height at ignition. Hydrogen jet flame was the subject of a thorough reevaluation by Molkov and Saffers [10]. An updated dimensionless flame length connection in terms of Froude, Reynolds, and Mach numbers is introduced. The probability density function (PDF) approach was first presented for pulverized coal combustion by Zhao and Haworth [11]. The researchers used the P-1 model to simulate radiative heat transfer for a gas-particle system that generates gray absorbance and scattering. In Hefei city at normal atmospheric pressure (100 kPa) and Lhasa city at sub-atmospheric pressure (64 kPa), Zhang *et al.* [12] performed experiments and presented mathematical modelling of the flame shape and gaseous fuel volume for turbulent jets issued through nozzles of varying diameters (4-6 mm and 8 mm) utilizing Propane fuel. The proposed model was illustrated to expect the flame volume in both pressures reasonably well, while the estimates were slightly larger than the experimental data.

Kang *et al.* [13] studied the dimethyl ether (DME) jet diffusion flame's $NO_x$ and CO emission experimentally and numerically using 2-D-CFD simulation. Reaction rate and vulnerability analyses were used to investigate the nitrogenous species adaption relationship, $NO_x$ generation, consumption pathways, and $NO_x$ and CO release trajectories of the DME-air jet diffusion flame. In a laboratory-scale oven equipped with a slot-type burner, Oh and Noh [14] conducted experimental research into the effect of altering the oxidizer and fuel construction on flame behavior. Both the fuel-to-oxidizer mass-flow rate and the equivalency ratio affected the flame pattern. Miltner *et al.* [15] performed an experimental and numerical examination of the flow field of a straight and a little rotating turbulent free jet using several turbulence models. The numerical results demonstrated the efficacy of numerical modelling in accurately describing the flow type under study. The jet diffusion flame's length, $L_f$, width, $W_f$, and volume, $V_f$, were investigated both experimentally and theoretically by Kang *et al.* [16]. The experimental investigation used a variety of fuel nozzle diameters, $d_f$, fuel jet velocities, $u_f$, and air co-flow air velocities, $u_{co}$, to examine the effects of these variables on flame characteristics. We found that the flame shape changed depending on the Reynolds number of the jet fuel. Experimental measurements and comparisons were made by Zhang *et al.* [17] of the soot-free length fraction (SFLF) of buoyant, non-premixed, turbulent jet flames at standard atmospheric pressure (100 kPa) and specifically a sub-atmospheric pressure (64 kPa). For a particular heat release rate, the SFLF increased with the heat issue rate but decreased with the growing nozzle of fuel diameter, with the maximum SFLF occurring at sub-atmospheric pressure.

Mardani *et al.* [18] investigated CO and $CO_2$ production for a $CH_4/H_2$ fuel combination underneath MILD combustion conditions of a jet in a hot coflow (JHC) burner. This study uses CFD. In an axisymmetric 2-D computing domain, the RANS equations with modified $k$-$\varepsilon$ equations are solved. The $CH_4$ oxidation routes are examined using oxidizer oxygen concentration and fuel hydrogen content. Under MILD conditions, greater hydrocarbon oxidation routes create CO and $CO_2$. Elattar *et al.* [19, 20] used a 2-D axisymmetric model to study rotary kiln restricted non-premixed jet flames. The Realizable $k$-$\varepsilon$ turbulent model suited well with theoretical and experimental data for non-premixed jet flames simulation. Fuel, surplus air number, air inlet diameter, temperature, and radiation modelling substantially affect rotary kiln flame length and peak flame temperature.

Recently, Liu *et al.* [21] introduced a coupling study among radiative heat transfer and combustion in modelling turbulent flame. Sun *et al.* [22] reported the 1-D first-order spherical harmonics P-1 non-gray radiation heat transfer technique in a gas with a spherical geometry. Except for gas mixing circumstances, the results reveal that the P-1 approach was just as accurate as the discrete ordinates method. The effects of radiation models on both stable and unstable laminar non-premixed flames were shown by Wu and Zhao [23]. Radiation solvers and spectrum models used in conjugate combustion-radiation simulations yielded nearly identical results for the two smaller flames. When soot was factored in, radiative re-absorption has a far more meaningful effect on the overall flame configuration of the two unstable flames. Kim and Kim [24] looked at how different absorption coefficient models affected the P-1 radiation model for a hydrogen-water vapor premix flame.

Based on reviewing the previous works, it is found that several numbers of research have been conducted to investigate the flame length characteristic experimentally and numerically. Whereas only a few works undertake CFD analysis for free jet flame without considering the impact of radiation modelling on the flame behavior (*i.e.*, length, shape, temperature*, etc.*) as well as computational time and cost. Moreover, further research is needed to determine the impacts of various operational factors, such as air temperature, fuel velocity, and gaseous fuel

types, on the flame length for turbulent non-premixed free jet flames. As a result, the current work aims to provide a computational analysis for the non-premixed free jet flame using the commercial code ANSYS-FLUENT 14.5 to investigate the effects of thermal radiation using the P-1 radiation model, air temperature, fuel velocity, and fuel type on flame length behavior. Such characteristics are required for the effective design and operation of the variable jet flame industrial process in order to manage the flame length, which regulates the thermal processes and, as a result, the product characteristic. Furthermore, mean mixture percentage and temperature contours are shown to help picture the flame form. Finally, as a primary contribution of the present study, useful design recommendations and dimensionless correlations that describe the flame length are established and provided while taking radiation modelling into account.

## Computational model geometry, details, and mesh

For studying the influence of the radiation model and operating parameters (air temperature, fuel velocity) on the flame behavior of a free turbulent jet, fig. 1 shows the schematic diagrams for the physical model, computational domain, and mesh boundary types used in the present free jet flame simulation. Figure 1(a) depicts the burner geometry of a pilot plain tube burner with a nozzle of 50 mm in diameter and a thermal power variety of 2.31-6.56 MW, depending on the fuel type. The fuel moves steadily from 30-100 m/s in the scenario. Table 1 summarizes the physical and thermal parameters of the fuels, with a focus on the three recommended gases: $CH_4$, CO, and biogas (50% $CH_4$ and 50% $CO_2$).

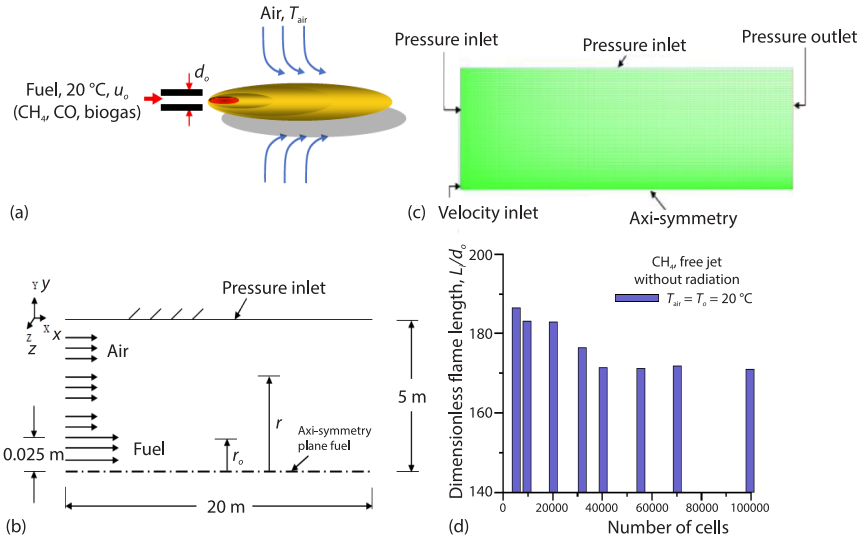


**Figure 1. The 2-D free jet flame model; (a) physical model schematic, (b) computational domain, (c) mesh and boundary types, and (d) mesh independence study**

**Table 1. Fuels' physical and thermal characteristics**

| Fuel kind | $L$ [$kg_{air}kg_o^{-1}$] | $\rho_o$ (20 °C) [$kgm^{-3}$] | $h_u$ (net) [$MJkg_o^{-1}$] | $M_o$ (kg/kmole) | $\tilde{L}$ [$m^3_{air}m^{-3}_o$] | $f_{st}$ | $K$ [$Wm^{-1}K^{-1}$] |
|---|---|---|---|---|---|---|---|
| $CH_4$ | 17.3 | 0.668 | 50 | 16 | 9.5 | 0.055 | 0.035 |
| Biogas | 5.45 | 1.248 | 20.5 | 30 | 4.76 | 0.155 | 0.0295 |
| CO | 2.46 | 1.165 | 10.1 | 28 | 2.38 | 0.289 | 0.24 |

The present simulation's 2-D domain geometry and mesh are displayed in figs. 1(b)-1(d). We assumed that the domain geometry of the free jet problems was a giant symmetrical cylinder to better depict a large room and eliminate the influence of impediments on flame behavior (length: 20 m, diameter: 10 m). As illustrated in fig. 1(b), half-cylinders have been used as a simulation domain to speed up calculations. Mesh and boundary conditions are shown in fig. 1(c). The flame zone around the burner contains 40400 organized and quadrilateral cells. The air input is a known pressure inlet, while the fuel intake is a velocity inlet. Combustion gas production is pressure. For mesh-size independence, many meshes are created. Flame length converges with mesh number, according to mesh independence research. To ensure flame length convergence as meshes grow, mesh independence research is done. The flame length convergence test employed meshes of 5270-99660 cells, as shown in fig. 1(d). As seen in the illustration, a mesh size more than 40400 cells usually produces a flame length fluctuation of 0.3% or less. 40400 meshes are utilized for simulations.

## Methodology

### *Choice and validation of turbulence model*

For the present simulation, *k-ε* slandered, *k-ε* RNG, *k-ε* realizable, *k-ω* standard, *k-ω* SST, and RSM turbulence models are employed. Simulation findings are compared with experimental data. Figures 2(a) and 2(b) compare axial mean mixture fraction and axial temperature profiles to experimental data [25], as reported by Elattar *et al*. [19, 20]. It is found that the *k-ε* (realizable) turbulence model is closest to experimental results with maximum errors of 33% (underestimation) and 22% (overestimation) for axial mean mixture fraction and axial temperature distributions, respectively. Therefore, the *k-ε* (realizable) is recommended to carry out the current simulations.

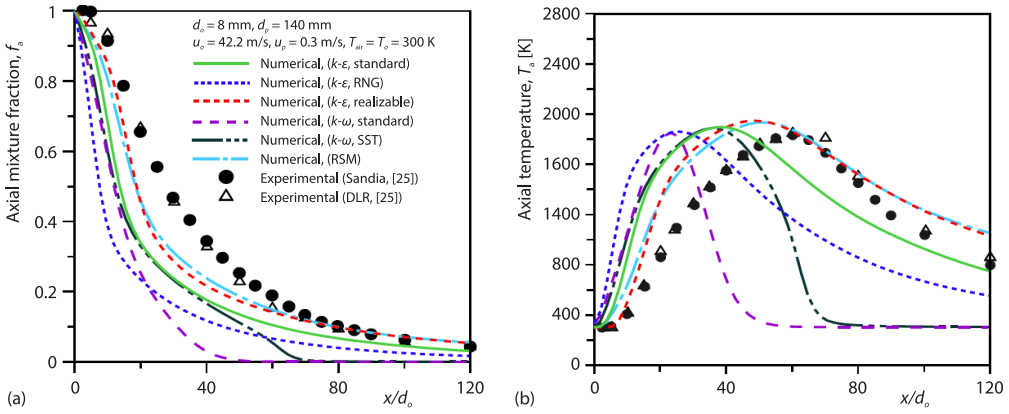


**Figure 2. Comparisons between several turbulence models and experimental results [25]; (a) axial mixture fraction and (b) axial temperature [19, 20]**

### *Mathematical models, formulations, and assumptions*

This work simulates RANS equations, species transport, energy equation, and radiation model in cartesian co-ordinates using a CFD realizable *k-ε* turbulent heat transfer and flow solver. These equations and models are in [21, 22, 26, 27]. Compared to existing *k-ε*, it saves computing time and correctly predicts the curved and swirling flow [28]. The 2nd order upwind interpolation approach is used to discretize the governing equations, and the SIMPLE algorithm

is used to couple pressure and velocity for a residual of continuity, momentum, and energy are smaller than $10^{-4}$, $10^{-5}$, and $10^{-6}$, respectively, then the solutions have converged, and the results can be confidently asserted. Chemical reaction modelling employs PDF and combustion models (non-premixed). Due to its turbulent mixing qualities, the PDF is recommended for turbulent flow in combustion processes, including fuel and oxidant streams. The $\beta$-PDF model is used in the current work because it gives clearer results for turbulent non-premixed combustion flow than other PDF models [29]. The mixture fraction, $f$, in the presumable $\beta$-PDF depends on species $I$ mass fraction, $Z_i$, which makes it easier to determine the species transport equation:

$$f = \frac{Z_i - Z_{i,\mathrm{ox}}}{Z_{i,\mathrm{fuel}} - Z_{i,\mathrm{ox}}} \tag{1}$$

where subscript ox is the oxidizer inlet value, and the subscript fuel indicates the fuel stream inlets.

The transport formulations of the mean mixture fraction, $\overline{f}$ and its variance, $\overline{f}'^2$ are illustrated in:

$$\frac{\partial}{\partial t}\left(\rho\overline{f}\right) + \frac{\partial}{\partial x_j}\left(\rho u_j \overline{f}\right) = \frac{\partial}{\partial x_j}\left(\frac{\mu_t}{\sigma_t}\frac{\partial \overline{f}}{\partial x_j}\right) \tag{2}$$

$$\frac{\partial}{\partial t}\left(\rho\overline{f}'^2\right) + \frac{\partial}{\partial x_j}\left(\rho u_j \overline{f}'^2\right) = \frac{\partial}{\partial x_j}\left(\frac{\mu_t}{\sigma_t}\frac{\partial \overline{f}'^2}{\partial x_j}\right) + C_{\mathrm{g}}\mu_t\left(\frac{\partial \overline{f}}{\partial x_j}\right)^2 - C_d\rho\frac{\varepsilon}{k}\overline{f}'^2 \tag{3}$$

where $f' = f - \overline{f}$, the constants are: $\sigma_t = 0.85$, $C_g = 2.86$, and $C_d = 2.0$. The mixture fraction is independent of any thermochemical scalar, species fraction, density, or temperature at the chemical equilibrium state. Instantaneous values of mass fraction, density, and temperature are directly related to the instantaneous mixture fraction, $f$, and are given:

$$\varphi_i = \varphi_i\left(f\right) \tag{4}$$

$$\varphi_i = \varphi_i\left(f, H\right) \tag{5}$$

Equations (4) and (5) represent instantaneous species mass fraction, density, or temperature, for adiabatic and non-adiabatic systems, respectively, and instantaneous enthalpy, denoted by $H$. Equations (6) and (7) provide the average species mass percent and temperature, $\overline{\varphi}_i$, in the case of adiabatic and non-adiabatic system, respectively:

$$\overline{\varphi}_i = \int_0^1 p\left(f\right)\varphi_i\left(f\right)\mathrm{d}f \tag{6}$$

$$\overline{\varphi}_i = \int_0^1 p\left(f\right)\varphi_i\left(f, \overline{H}\right)\mathrm{d}f \tag{7}$$

Accordingly, the mean time-averaged fluid density $\overline{\rho}$ can be determined:

$$\frac{1}{\overline{\rho}} = \int_0^1 \frac{p\left(f\right)}{\rho\left(f\right)}\mathrm{d}f \tag{8}$$

where

$$p(f) = \frac{f^{\alpha-1}(1-f)^{\beta-1}}{\int f^{\alpha-1}(1-f)^{\beta-1}\mathrm{d}f}$$

where $\alpha$ and $\beta$ are:

$$\alpha = \overline{f}\left[\frac{\overline{f}\left(1-\overline{f}\right)}{f'^2}-1\right],\ \beta = \left(1-\overline{f}\right)\left[\frac{\overline{f}\left(1-\overline{f}\right)}{f'^2}-1\right]$$

For solving the mean enthalpy, $\overline{H}$ transport equation and predict $\overline{\varphi}_i$. For the non-adiabatic system:

$$\frac{\partial}{\partial t}\left(\rho\overline{H}\right)+\nabla\left(\rho\vec{v}\overline{H}\right)=\nabla\left(\frac{k_t}{c_p}\nabla\overline{H}\right) \tag{9}$$

The species' thermal characteristics are expressed in terms of temperature and normal atmospheric pressure ($1.013 \cdot 10^5$ Pa). For the enthalpy solution, energy equation is used:

$$\frac{\partial}{\partial x_i}\left(\rho v_i h\right)=\frac{\partial}{\partial x_i}\left(\Gamma_h\frac{\partial h}{\partial x_i}\right)+S_h \tag{10}$$

Combustion and radiation heat transfer rates are included in tsource variable $S_h$ in eq. (10).

The P-1 radiation model calculates free jet flame radiation flux. The P-1 radiation models are simpler than P-N models [30, 31]. The P-1 model also requires few CPU working units and may be considered in intricate geometries. A useful indicator of the model to utilize in the current study is the optical thickness $\alpha L$. Here, $L$ is an appropriate length scale for the computational domain. If $\alpha L \gg 1$, the best alternatives are the P-1 and Rosseland models. The P-1 model should typically be used for $\alpha L > 1$ [28]. For $\alpha L > 3$, the Rosseland model is cheaper and more efficient. Both the discrete transfer radiation model (DTRM) and the discrete ordinates (DO) radiation model are effective across a wide range of optical thicknesses, but they come at a high price. If the issue permits it, we should thus use *thick-limit* models such as P-1 and Rosseland. Only the DTRM and the DO model are valid for optically thin issues ($\alpha L < 1$) [28]. Gaseous fuel simulations assume isotropic scattering coefficients of zero. The computational domain's mean absorption coefficient is ≅ 0.4 1/m, $L = 5$ m, and $\alpha L$ is ≅ 2. Thus, the P-1 model suits this work. Local $H_2O$ and $CO_2$ concentrations, route length, and pressure determine the absorption coefficient. Equation (11) calculates α using a weighted-sum-of-gray-gases model (WSGGM):

$$q_r = -\Gamma\nabla G \tag{11}$$

where $G$ is the incident radiation and $\Gamma$ – the introducing parameter and described:

$$\Gamma = \frac{1}{3\left(\alpha+\sigma_s\right)-C\sigma_s} \tag{12}$$

where $\alpha$ is the absorption coefficient, $\sigma_s$ – the scattering coefficient, and $C$ – the linear anisotropic phase function coefficient, the transport equation for $G$:

$$\nabla\left(\Gamma\nabla G\right)-\alpha G+4\alpha n^2\sigma T^4 = S_G \tag{13}$$

where $n$ is the medium refractive index and $S_G$ – the user-defined radiation supply. Combining eqs. (11) and (13) yields:

$$-\nabla q_r = \alpha G - 4\alpha n^2 \sigma T^4 \tag{14}$$

To determine the heat sources/sinks owing to radiation, the $-\nabla q_r$ may be easily replaced with the energy equation. Indeed, CFD and commercial software are now essential tools in developing several engineering applications [32-36]. Thus, FLUENT has been used to simulate all configurations in this work.

## Results and discussion

### *Species distributions and effects of fuel velocity*

Figure 3(a) depicts typical mass fraction patterns along the flame centerline during $CH_4$ combustion without radiation modelling effects. As shown in the figure, $CH_4$ mass fraction reduces along the flame owing to CO conversion $CO_2$ is still uncompleted. The hydrocarbon flames are ended when there is no CO in the flame axis. Figure 3(b) shows radial patterns of species mass fractions at $x/d_o = 30$. A reaction zone is emerging because oxygen and methane coexist. The effects of varying the fuel velocity, $u_o$, from 30-150 m/s on the centerline axial temperature profiles, $T_a$, and the centerline inverted mean mixture percent, $f_a$, were shown without taking radiation modelling into account in figs. 4(a) and 4(b). The fuel and air temperatures were both 20 °C. At any given fuel velocity, as shown in fig. 4(a), the flame temperature rises along the flame axis until it reaches its maximum (≈1800 °C) at $x/d_o = 170$, after which it decreases along the flame axis. The figure also shows that the axial flame temperature profiles are unaffected by $u_o$. While fig. 4(b) shows the inverted axial mean mixture fraction along the flame axis. The flame length reaches its maximum when the simulated mean fraction matches the stoichiometric mean mixture fraction, $f_{st}$. At $x/d_o = 174$, methane's free jet flame length ended. Additionally, since all of the analyzed situations fall within the range of turbulent flame, the flame duration is independent of the fuel velocity and, as a result, the thermal power of the burner. This conclusion is consistent with Yang and Blasiak [37], where the fuel's Reynolds numbers vary from Re = 91363-487500.

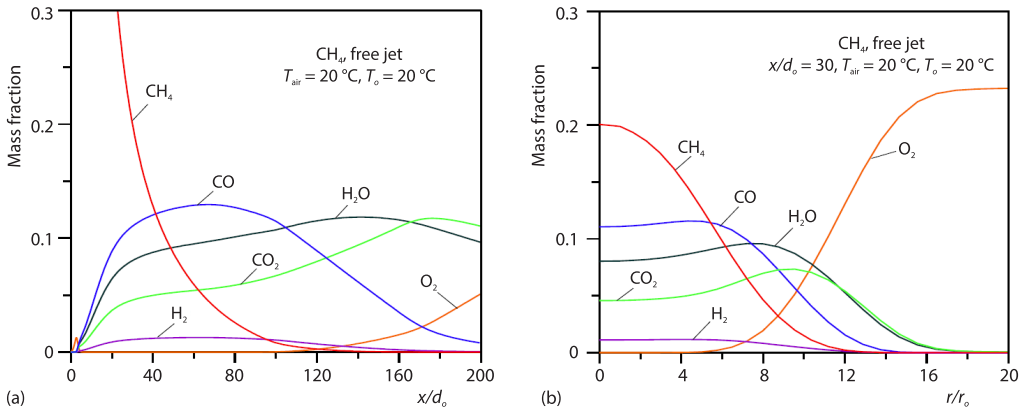


**Figure 3. Species mass fraction distributions; (a) axial distribution and (b) radial distribution**

### *Effects of air temperature*

The impacts of air temperature, $T_{air}$ (20-1000 °C) on $u_a$, $T_a$, $f_a$, and axial flame density, $\rho_a$ *vs.* mean mixture fraction are shown in figs. 5(a)-5(d) using $CH_4$ fuel at $u_o = 100$ m/s and $T_o = 20$ °C. In this case, the radiation model (P-1) was not considered in the simulation (without

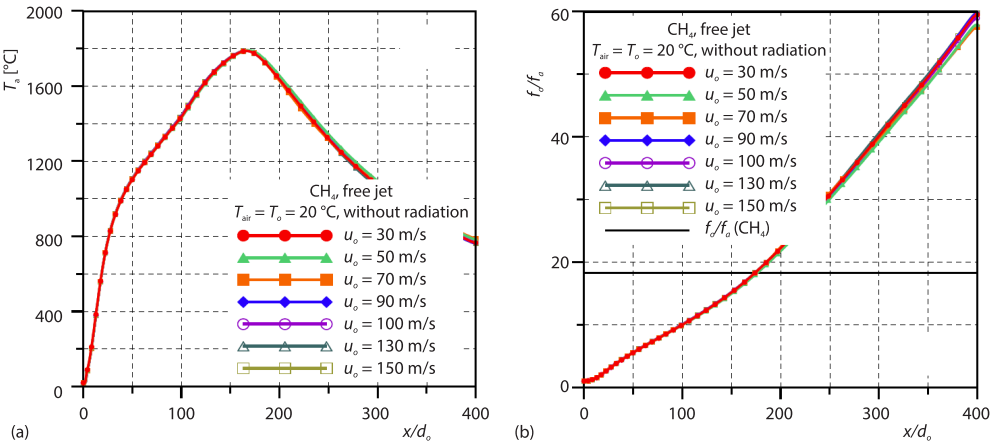


**Figure 4. Influence of fuel velocity on; (a) axial temperature distribution and (b) inverted axial mean mixture fraction**

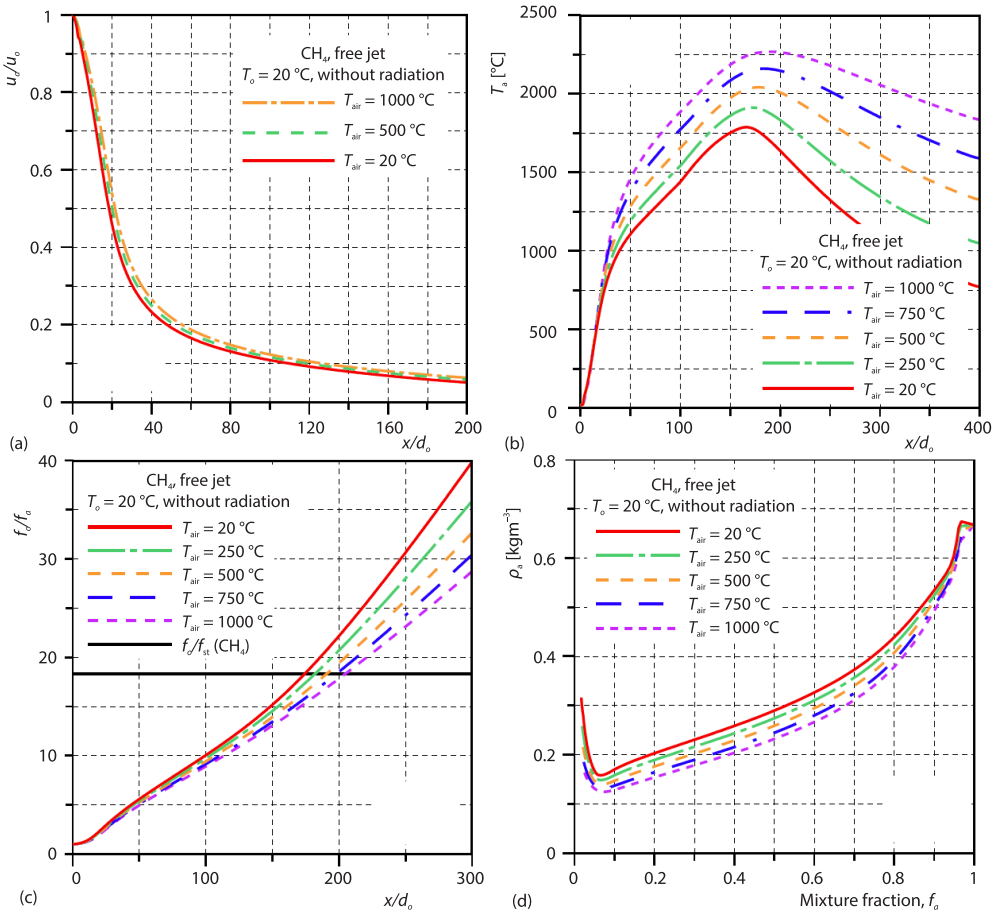


**Figure 5. Influence of air temperature on; (a) axial velocity, (b) axial temperature, (c) inverted axial mixture fraction, and (d) axial $CH_4$ density *vs.* axial mixture fraction**

radiation). In fig. 5(a), we see how the axial flame velocity ($u_a/u_o$) is affected by air temperatures of 20 °C, 250 °C, and 1000 °C. The figure indicates axial flame speed seldom varies with air temperature and even rises. As the picture shows, axial velocity decreases along the flame axis, as expected. Elattar [20] said this affects fuels with more significant stoichiometric mean mixing percentages. Figure 5(b) shows how $T_{air}$ affects $T_a$ along the flame axis. Axial flame temperature profiles show air temperature's influence.

Where the axial flame temperature distribution increases with increasing air temperature, this can be ascribed to the growth of air temperature (oxidizer) tends to increase the combustion gas mixing temperature. Accordingly, a rise in flame temperature is observed. Moreover, the peak flame temperature increases by ≈28% with increasing $T_{air}$ from 20-1000 °C. Figure 5(c) shows how the value of $T_{air}$ affects the length of the free jet flame. With growing air temperature, $T_{air}$, the mass flux is reduced by turbulent mixing due to the air's decreasing density. Therefore, the flame ends when the simulated $f_a$ equals the stoichiometric mean mixture fraction, $f_{st}$, see fig. 5(c). The low density means fewer oxidants can diffuse into the fuel flow, less air can enter the fuel jet, and the flame must travel farther to finish the reaction, increasing the flame length to complete the reaction process at a higher temperature. Yang and Blasiak [37] conducted an identical study. Also, it is shown that a temperature rises from 20-1000 °C in the air results in a lengthening of the flame by around 18%. Figure 5(d) illustrates the variation of $\rho_a$ against $f_a$ with different $T_{air}$. As shown in the figure, the flame density reduces with raising $f_a$ to the lowest value at $f_{st}$ then it increases with $f_a$, and the same trend is observed at any air temperature. This can be ascribed to increasing the flame temperature with the increase of mean mixture fraction until it reaches the peak flame temperature at $f_{st}$, since the fuel convergence is improved. As a result, the flame density decreases until it reaches its lowest point at the highest flame temperature. Following the peak flame temperature, the flame temperature drops as $f_a$ rises, which causes the flame density to rise once again. Moreover, the flame density distribution against $f_a$ decreases with the air temperature rise, and this effect is sensible at low $f_a$ and trivial

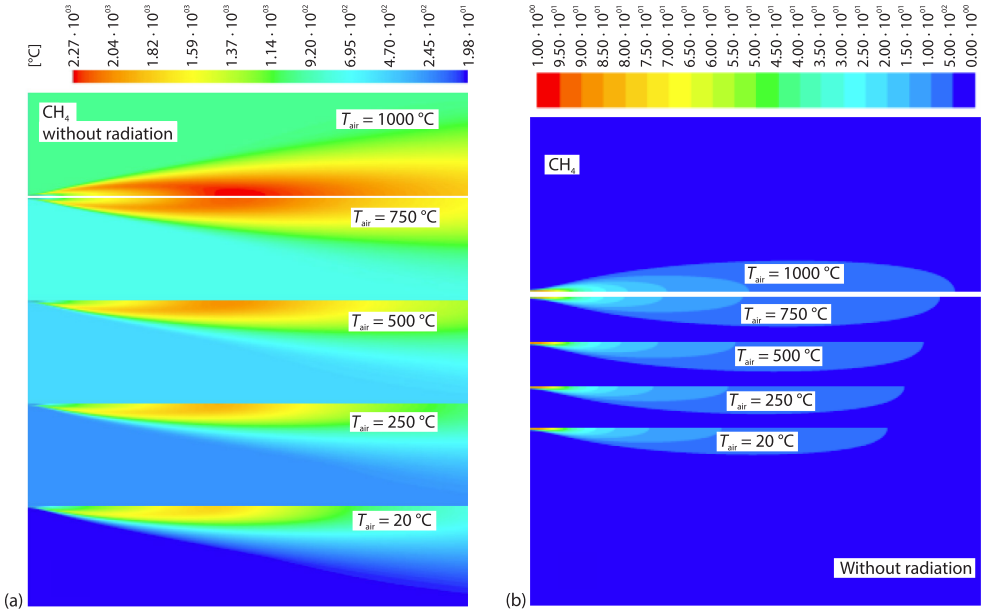


**Figure 6. Influence of $T_{air}$ on; (a) temperature contours and (b) mixture fraction contours**

at high $f_a$. Figures 6(a) and 6(b) demonstrate how ambient temperature affects $CH_4$ temperature and mean mixture fraction contours fig. 6(b). The outlines show that air temperature influences peak flame temperature and length.

### *Effects of radiation modelling*

The influences of radiation modelling (with and without radiation) on $T_a$, $f_a$, $\rho_a$, and on temperature and mean mixture fraction contours are described in fig. 7(a)-7(f) using $CH_4$ fuel at $u_o$ = 100 m/s, $T_o$ = 20 °C, and different $T_{air}$ (20 °C, 500 °C, and 1000 °C) as a studied parameter. In this study, the radiation model (P-1) is used (*i.e.*, in case of radiation impact), and the results *with radiation* are compared with the case of *without radiation* modelling. Radiation modelling impact on the axial flame temperature profiles is depicted in fig. 7(a). As seen in the figure for any $T_{air}$, *with radiation* reduces the distribution of the axial flame temperature and peak flame temperature (*i.e.*, with radiation modelling). The flame cools and the temperature profile along the flame drops owing to radiation heat adding to the flame's total heat output. The figure also demonstrated that radiation modelling affects axial flame temperature more for higher $T_{air}$ and less for lower $T_{air}$. Radiation only provides a little amount of heat transfer at low air temperatures. Hence it very marginally affects the axial flame temperature profile. The $CH_4$ fuel flame temperature contours at 20 °C are illustrated in fig. 7(b). Radiation modelling is associated with the flame zone's lower temperatures, as seen in the picture. Figure 7(c) shows how radiation modelling might affect flame length estimation using inverted dimensionless axial mean mixture fraction profiles, $f_o/f_a$. As can be seen, the radiation modelling has adversely affected the flame length. The flame length shortens with radiation modelling due to cooling the flame, which leads the flame to complete its reaction in a short distance due to its higher density. Moreover, the figure shows that at lower $T_{air}$, the influence of radiation modelling on the flame length is small, whereas, at higher $T_{air}$, it is reasonable. This is due to the explanation given in fig. 5(c). Furthermore, in the case of radiation modelling, the $CH_4$ flame length short-

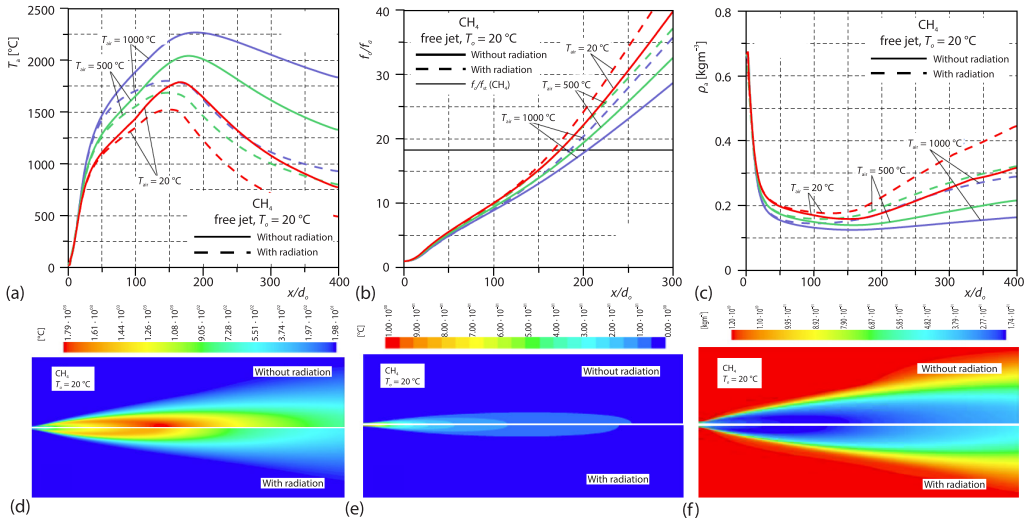


**Figure 7. Influence of radiation modelling on; (a) axial temperature profiles, (b) temperature contours, (c) axial mixture fraction profiles, (d) mixture fraction contours, (e) axial $CH_4$ density profiles, and (f) $CH_4$ fuel density contours**

ens by 4%, 9%, and 10% at 20 °C, 500 °C, and 1000 °C air temperatures. Figure 7(d) indicates the impact of radiation on the flame average mixture fraction contours for $CH_4$ fuel at 20 °C air temperature. As illustrated in the figure, the radiation modelling has a tiny effect on flame length shortening (*i.e.*, at small ambient temperatures). Figure 7(e) shows radiation's impact on axial flame density, $\rho_a$ profiles, where the radiation modelling moved up the $\rho_a$ profile at any air temperature. This can be attributed to the amount of heat part transferred during radiation modelling, which lowers the flame temperature and consequently increases the flame density. Moreover, the impact of radiation modelling on $\rho_a$ reduces at lower $T_{air}$ and is negligible at lower fuels' heating values, such as biogas and CO, as reported by Elattar [20]. Additionally, fig. 7(f) illustrates that a flame with a greater density zone is associated with radiation modelling.

### *Fuel comparisons*

The comparison between three gaseous fuels ($CH_4$, biogas, and CO) at $u_o$=100 m/s, $T_o$= 20 °C on the flame behavior is presented in the following sections. Figures 8 and 9 show the influence of the kind of fuel on $u_a/u_o$, $T_a$, $f_o/f_a$, $(f_a - f_{st})/(f_o - f_{st})$ profiles, temperature, and mean mixture fraction contours. A comparison between present numerical and literature analytical results for flame length and radial velocity distribution is also presented.

Figure 8(a) shows $CH_4$, biogas, and CO axial velocity profiles at 20 °C. As seen, axial velocity decreases along the flame axis for all fuels. The CO has the greatest velocity profile up to $x/d_o \approx 40$, whereas $CH_4$ has the lowest. The higher fuel density results in a higher axial velocity profile, see tab. 1. Whereas the velocity profile of CO is higher than $CH_4$, and biogas has an intermediate velocity profile, after $x/d_o \approx 100$, fuel type has negligible influence on velocity profiles. The axial temperature profiles for the studied fuels are also presented in figs. 8(b) and 8(c) with and without radiation modelling consideration at $T_{air}$= 20 °C. As displayed in fig. 8(b), CO has the ultimate peak flame temperature located at $x/d_o \approx$ (41-47) based on $T_{air}$ and the impact of radiation modelling, but biogas has the smallest peak flame temperature located at $x/d_o \approx$ (71-86), and $CH_4$ in between and located at $x/d_o \approx$ (166-205). The CO has the highest peak flame temperature and shortest flame length, whereas $CH_4$ has the middle peak temperature and longest flame length. Radiation does not affect CO and biogas temperature distribution (*i.e.*, lower heating value fuels). Radiation modelling and non-radiation modelling axial temperature profiles for all fuels throughout the flame length (limited with flame end) are illustrated in fig. 8(c). As seen in the image, both *with radiation* and *without radiation* conditions have a peak flame temperature towards the flame end. So, the flame ends at the greatest flame temperature when the mean mixture percent is stoichiometric according to the method of flame length calculation.

Additionally, fig. 8(d) and 8(e) display $f_o/f_a$ and $(f_a - f_{st})/(f_o - f_{st})$ profiles along the flame axis for $CH_4$, biogas, and CO fuels at $T_{air}$= 20 °C, with and without radiation simulation consideration. As shown in fig. 8(d), the flame ends where the simulated mean mixture fraction equals the stoichiometric value. As the fuel stoichiometric mean mixture decreases, the flame lengthens, see tab. 1. As observed, CO has the lowest flame length, followed by $CH_4$ and biogas, with $CH_4$ having the maximum flame length both *with radiation* and *without radiation*. Without radiation modelling, $CH_4$ has 59% and 76% longer flames than CO and biogas. Figure 8(e) illustrates the axial mixture fraction profiles along the flame lengths of all fuels. For all fuels, the axial mean mixture fraction drops to the stochiometric value at the flame end, *i.e.* $(f_a - f_{st})/(f_o - f_{st})$= 0 at the flame end). Figiure 9(a) compares the analytical flame length cor-

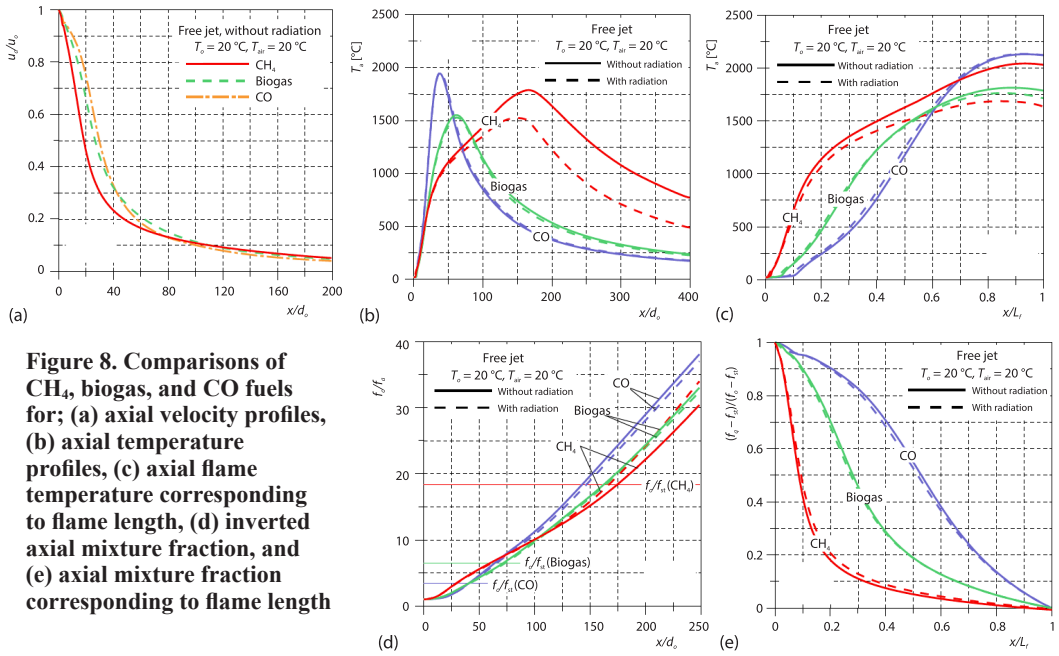


**Figure 8. Comparisons of $CH_4$, biogas, and CO fuels for; (a) axial velocity profiles, (b) axial temperature profiles, (c) axial flame temperature corresponding to flame length, (d) inverted axial mixture fraction, and (e) axial mixture fraction corresponding to flame length**

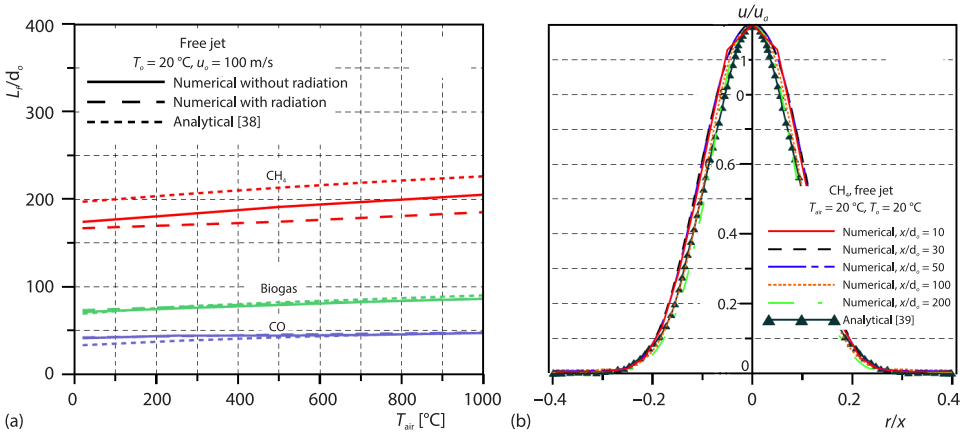


**Figure 9. Comparison of present numerical and analytical results; (a) flame length [38] and (b) velocity profiles [39]**

relation of Specht [38] (where $L_f/d_o = 1/(f_{st} \tan 9°)(\rho_o/\rho)^{0.5}$) with the current simulated free jet flame length *with radiation* and *without radiation* for $CH_4$, biogas, and CO fuels at 100 m/s fuel velocity and 20 °C fuel temperature. The simulated free jet flame lengths for biogas and CO fuels fit well with the analytical solution, while the analytical $CH_4$ solution is 12% higher than the numerical solution. This difference is due to the modelling assumptions and numerical approximations. Figure 9(b) compares the radial dimensionless velocity patterns between current numerical results and analytical results reported by Giese [39] using $CH_4$ fuel at 20 °C and air temperature of 20 °C, where the radial velocity profiles are simulated at dissimilar distances from the burner tip ($x/d_o$=10, 30, 50, 100, and 200). The comparison illustrates good agreement

between the analytical solution [39] and the present numerical simulation, confirming the validation of the current simulation approach.

### Correlations between velocity and flame length

From the simulation findings of the present study, regression analysis yields the following inverted dimensionless axial velocity correlation in terms of axial distance from burner tip, nozzle diameter, average jet flame density, and fuel density:

$$\frac{u_o}{u_o} = 0.1597 \frac{x}{d_o} \sqrt{\frac{\rho}{\rho_o}} \tag{15}$$

where $\rho$ is the mean centerline jet density along the flame. Equation (15) was obtained from data in the following ranges: 20 °C ≤ $T_{air}$ ≤ 1000 °C, 10 ≤ $x/d_o$ ≤ 200, and $T_o$ = 20 °C. The prediction of this equation is shown in fig. 10(a). The correlation can describe 85% of numerical results within an error of ±15%.

From the present study's computed results, regression analysis can be used to derive the dimensionless free jet flame length in terms of stoichiometric air demand (mass basis):

$$\frac{L_f}{d_o} = 14.14\left(1+L\right)^{0.86} \tag{16}$$

Equation (16) is achieved from data in the following ranges: 2.46 ≤ $L$ ≤ 17.3, $T_{air}$ = 20 °C, and $T_o$ = 20 °C. The estimate of this equation is shown in fig. 10(b). The correlation can predict 100% of the numerical results within an error of ±0.73%. A second flame length correlation over a large air temperature range is produced. Fuel density, stoichiometric density, and mean mixture percentage affect dimensionless flame length:

$$\frac{L_f}{d_o} = \frac{4.8}{f_{st}} 14.14 \left(\frac{\rho_o}{\rho_{st}}\right)^{1/2} \tag{17}$$

Equation (17) is valid for data in the following ranges: 0.055 ≤ $f_{st}$ ≤ 2.89, 20 °C ≤ $T_{air}$ ≤ 1000 °C, and $T_o$ = 20 °C. The prediction of this correlation is shown in fig. 10(c). The correlation can predict 100% of the numerical results within an error of ±9.5%. When determining the density ratio $\rho_o/\rho_{st}$ for the flame length eq. (17), we can set the molecular weight at a stoichiometric mixture equal to Nitrogen [40]:

$$\frac{\rho_o}{\rho_{st}} = \frac{M_o}{M_{N_2}} \frac{T_{st}}{T_o} \tag{18}$$

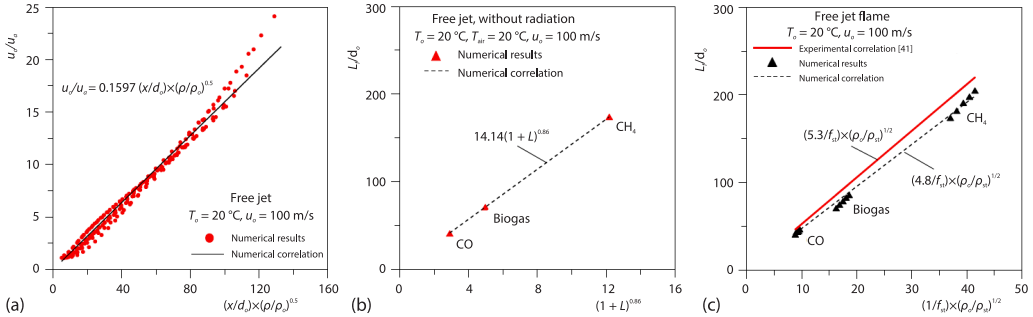


**Figure 10. Free jet flame correlations prediction; (a) fuel axial velocity, (b) flame length, and (c) comparison with [41]**

Here, $T_{st}$ is the combustion gas temperature at the stoichiometric mixture, so the maximum flame temperature is assumed. The $T_{st}$ equals 2061 K, 1825K, and 2217 K for $CH_4$, biogas, and CO, respectively, at $T_{air}$= 20 °C and $T_o$ = 20 °C. The extreme deviation achieved amongst numerical correlation eq. (17) and its approximation using eq. (18) is ±8%. Figure 10(c) compares Hawthorne *et al.* [41] experimental correlation the current numerical correlation, eq. (17). Experimental flame length is longer than simulated, but no significant deviations are noticed. This is due to the difference in definitions of the flame length for both simulated and measured values. Moreover, experimental and simulated findings differ due to turbulence and combustion models' simplifying assumptions and measurement uncertainty. The highest variation between experimental correlation [41] and the numerical one, eq. (17), is 9.4%.

## Conclusions

Three gaseous fuels ($CH_4$, biogas, and CO) were used in 2-D CFD simulations for free jet flame using the commercial CFD package ANSYS-FLUENT 14. The effects of radiation modelling using the P-1 model and other significant influencing parameters (fuel velocity, air temperature, and fuel type) were investigated and reported. The following is a summary of the key conclusions of the current work:

- The flame length and the peak flame temperature increase with increasing the air temperature (oxidant temperate), while the flame length is independent of the inlet fuel velocity (*i.e.*, burner power).
- Radiation significantly affects $CH_4$ fuel's flame duration and peak flame temperature, causing the flame temperature to decline and the flame length to shorten with radiation simulation. But the temperature distribution and flame durations for CO and biogas are unaffected by the radiation simulation (*i.e.*, lower heating value fuels).
- The $CH_4$ flame length shortens by 4%, 9%, and 10% at 20 °C, 500 °C, and 1000 °C air temperatures, respectively, in the case of radiation modelling.
- The CO had the greatest ultimate flame temperature and the shortest flame length of any of the fuels (*i.e.*, smallest flame volume). Compared to CO and biogas, $CH_4$ has the longest flame length (*i.e.*, the largest flame volume) and the intermediate peak flame temperature.
- The average flame density, fuel density, nozzle diameter, and axial distance from the burner tip were used to establish a general numerical correlation for $u_o/u_a$. Within an error of 15%, this connection may accurately predict 85% of computational outputs. Additionally, a dimensionless version of the general flame length correlation in stoichiometric air demand ($L_f/d_o$) on a mass basis was derived from computed data with a maximum inaccuracy of 0.73%. We also propose a dimensionless flame length correlation ($L_f/d_o$) that is a function of the proportion of the stoichiometric mixture, the density of the fuel, and the density of the stoichiometric mixture, which can account for 95% of the variation in numerical data.
- Within a maximum error of 9.4%, a comparison was made between the anticipated numerical flame length correlation and the experimental correlation accessible in the literature.
- The impact of different radiation models (Rosseland model, DTRM, DO*, etc.*) on the turbulent free jet flame behavior is recommended for future work.
- Investigations of burner geometry using different biofuels are also recommended for future studies on the industrial scale's characteristics of turbulent non-premixed jet flames.

## Declaration-of-competing-interests

The authors declare that they have no known competing financial interests or personal relationships that could have appeared to influence the work reported in this paper.

## Acknowledgment

The Fourth author would like to thank the Deanship of Scientific Research at Umm Al-Qura University for supporting his work by Grant No. 23UQU4361231DSR002.

## Nomenclatures

$d_o$ – fuel nozzle diameter, [m]
$f$ – mixture fraction
$G$ – radiation intensity, [Wm$^{-2}$]
$g_i$ – gravitational acceleration, [ms$^{-2}$]
$h_u$ – net heating value, [MJkg$_o^{-1}$]
$I$ – turbulence intensity
$k$ – turbulent kinetic energy, [m$^2$s$^{-2}$]
$L$ – stoichiometric air to fuel mass ratio, [kg$_{air}$/kg$_{fuel}$]
$\tilde{L}$ – stoichiometric air to fuel volume ratio
$L_f$ – overall jet flame length, [m]
$M_o$ – molecular weight, [kgkmol$^{-1}$]
$p$ – pressure, [Pa]
$q_r$ – radiation heat flux, [wm$^{-2}$]
$r_{a,i}$ – radius of air entrance, [m]
$T$ – temperature
$u$ – mean axial velocity, [ms$^{-1}$]
$V_f$ – overall jet flame volume
$W_f$ – overall jet flame width
$x$ – axial distance from burner, [m]
$Z_i$ – mass fraction of species $i$

*Greek symbols*

$\varepsilon$ – turbulent dissipation rate, [m$^2$s$^{-3}$]
$\alpha$ – absorption coefficient, [m$^{-1}$]
$\mu$ – dynamic viscosity, [Pa·s]
$\mu_t$ – turbulent viscosity, [kgm$^{-1}$s$^{-1}$]
$\nu$ – kinematic viscosity, [m$^2$s$^{-1}$]
$\rho$ – density, [kgm$^{-3}$]
$\sigma$ – Stefan-Boltzmann constant, [5.669·10$^{-8}$ Wm$^{-2}$K$^{-4}$]
$\varphi$ – equivalence ratio, [= (air/fuel)$_{st}$/(air/fuel)$_{actual}$]

*Subscript*

a – axial
air – air
o – fuel
st – stoichiometric

## References

[1] Fleck, B. A., *et al*., *Experimental and Numerical Investigation of the Novel Low $NO_x$ CGRI Burner,* Combust. Sci. Technol., *161* (2000), 1, pp. 89-112
[2] Schumaker, S. A., James F. D., Coaxial Turbulent Jet Flames: Scaling Relations for Measured Stoichiometric Mixing Lengths, *Proceedings of the Combustion Institute* (International Symposium on Combustion), *32* (2009), 2, pp. 1655-1662
[3] Elbaz, A. M., Roberts, W. L., Stability and Structure of Inverse Swirl Diffusion Flames with Weak to Strong Swirl, *Experimental Thermal and Fluid Science*, *112* (2020), 109989
[4] Mahmud, T., *et al*., Experimental and Computational Study of a Lifted, Non-Premixed Turbulent Free Jet Flame, *Fuel*, *86* (2007), 5-6, pp. 793-806
[5] Lawn, C. J., Lifted Flames on Fuel Jets in Co-Flowing Air, *Progress in Energy and Combustion Science*, *35* (2009), 1, pp. 1-30
[6] Houf, W. G., et al., Analysis of Jet Flames and Unignited Jets from Unintended Releases of Hydrogen, *International Journal of Hydrogen Energy*, *34* (2009), 14, pp. 5961-5969
[7] Jiang, F., *et al*., Flame Characteristics Influenced by the Angle of Burners for Non-Premixed $C_3H_8$/Air, *Thermal Science*, *26* (2022), 6B, pp. 5147-5156
[8] Choi, B. C., Chung, S. H., An Experimental Study on Turbulent Lifted Flames of Methane in Coflow Jets at Elevated Temperatures, *Fuel*, *103* (2013), Jan., pp. 956-962
[9] Oh, J., Noh, D., Lifted Flame Behavior of a Non-Premixed Oxy-Methane Jet in a Lab-Scale Slot Burner, *Fuel*, *103* (2013), Jan., pp. 862-868
[10] Molkov, V., Saffers, J.-B., Hydrogen Jet Flames, *International Journal Oo Hydrogen Energy*, *38* (2013), 19, pp. 8141-8158
[11] Zhao, X.-Y., Haworth, D. C., Transported PDF Modelling of Pulverized Coal Jet Flames, *Combustion and Flame*, *161* (2014), 7, pp. 1866-1882

[12] Zhang, X., *et al*., A Mathematical Model for Flame Volume Estimation Based on Flame Height of Turbulent Gaseous Fuel Jet, *Energy Conversion and Management*, *103* (2015), Oct., pp. 276-283
[13] Kang, Y., *et al.*, Experimental and Numerical Study on $NO_x$ and CO Emission Characteristics of Dimethyl Ether/Air Jet Diffusion Flame, *Applied Energy*, *149* (2015), July, pp. 204-224
[14] Oh, J., Noh, D., Flame Characteristics of a Non-Premixed Oxy-Fuel Jet in a Lab-Scale Furnace, *Energy*, *81* (2015), Mar., pp. 328-343
[15] Miltner, M., *et al*., The CFD Simulation of Straight and Slightly Swirling Turbulent Free Jets Using Different RANS-Turbulence Models, *Applied Thermal Engineering*, *89* (2015), Oct., pp. 1117-1126
[16] Kang, Y., *et al*., On Predicting the Length, Width and Volume of the Jet Diffusion Flame, *Applied Thermal Engineering*, *94* (2016), Feb., pp. 799-812
[17] Zhang, X. L., *et al*., Soot Free Length Fraction of Buoyant Turbulent Non-Premixed Jet Flames in Normal- and a Sub-Atmospheric Pressure, *Applied Thermal Engineering*, *110* (2017), Jan., pp. 111-114
[18] Mardani, A., *et al.*, Numerical Study of CO and $CO_2$ Formation in $CH_4/H_2$ Blended Flame under MILD Condition, *Combustion and Flame*, *160* (2013), 9, pp. 1636-1649
[19] Elattar, H. F., Flame Simulation in Rotary Kilns using Computational Fluid Dynamics, Ph. D. thesis, Magdeburg University, Magdeburg, Germany, 2011
[20] Elattar, H. F., *et al.*, The CFD Simulation of Confined Non-Premixed Jet Flames in Rotary Kilns for Gaseous Fuels, *Computers and Fluids*, *102* (2014), Oct., pp. 62-73
[21] Liu, F., *et al*., The Impact of Radiative Heat Transfer in Combustion Processes and Its Modelling – With a Focus on Turbulent Flames, *Fuel*, *281* (2020), 118555
[22] Sun, Y., *et al.*, The 1-D P-1 Method for Gas Radiation Heat Transfer in Spherical Geometry, *International Journal of Heat and Mass Transfer*, *145* (2019), 118777
[23] Wu, B., Zhao, X., Effects of Radiation Models on Steady and Flickering Laminar Non-Premixed Flames, *Journal of Quantitative Spectroscopy and Radiative Transfer*, *253* (2020), 107103
[24] Kim, S., Kim, J., Effect of Radiation Model on Simulation of Water Vapor – Hydrogen Premixed Flame Using Flamelet Combustion Model in OpenFOAM, *Nuclear Engineering and Technology*, *54* (2022), 4, pp. 1321-1335
[25] Meier, W., *et al*., Raman/Rayleigh/LIF Measurements in a Turbulent $CH_4/H_2/N_2$ Jet Diffusion Flame: Experimental Techniques and Turbulence – Chemistry Interaction, *Combustion and Flame*, *123* (2000), 3, pp. 326-343
[26] Elattar, H. F., *et al*., The CFD Modelling Using PDF Approach for Investigating the Flame Length in Rotary Kilns, *Heat and Mass Transfer*, *52* (2016), 12, pp. 2635-2648
[27] Elattar, H. F., *et al*., Study of Parameters Influencing Fluid-flow and Wall Hot Spots in Rotary Kilns Using CFD, *The Canadian Journal of Chemical Engineering*, *94* (2016), 2, pp. 355-367
[28] ***, ANSYS, Inc., ANSYS FLUENT User's guide. Ansys Inc, Canon-sburg, 2011
[29] Poinsot T., Veynante D., *Theoretical and Numerical Combustion,* (R.T. Edwards), Inc., Philadelphia, Penn., USA, 2001
[30] Cheng, P., The 2-D Radiating Gas-flow by a Moment Method, *AIAA Journal*, *2* (1964), 9, pp. 1662-1664
[31] Siegel, R., Howell, J. R., *Thermal Radiation Heat Transfer*, Hemisphere Publishing Corporation, Washington (DC), USA, 1992
[32] Waqas, H., *et al.*, Numerical and Computational Simulation of Blood Flow on Hybrid Nanofluid with Heat Transfer through a Stenotic Artery: Silver and Gold Nanoparticles, *Results in Physics*, *44* (2023), 106152
[33] Li, Z., *et al*., Heat Storage System for Air Conditioning Purpose Considering Melting in Existence of Nanoparticles, *Journal of Energy Storage*, *55* (2022), 105408
[34] Abidi, A., *et al.*, Improving the Thermal-Hydraulic Performance of Parabolic Solar Collectors Using Absorber Tubes Equipped with Perforated Twisted Tape Containing Nanofluid, *Sustainable Energy Technologies and Assessments*, *52* (2022), 102099
[35] Alqarni, M. M., *et al*., Two-Phase Simulation of a Shell and Tube Heat Exchanger Filled with Hybrid Nanofluid, *Engineering Analysis with Boundary Elements*, *146* (2023), Jan., pp. 80-88
[36] El-Amin, M. F., *et al*., Numerical Simulation and Analysis of Confined Turbulent Buoyant Jet with Variable Source, *Journal of Hydrodynamics*, *27* (2015), 6, pp. 955-968
[37] Yang, W., Blasiak, W., Chemical Flame Length and Volume in Liquified Propane Gas Combustion Using High-Temperature and Low-Oxygen-Concentration Oxidizer, *Energy and Fuels*, *18* (2004), 5, pp. 1329-1335
[38] Specht, E., *Heat and Mass Transfer in Thermoprocessing: Fundamentals | Calculations | Processes*, (Edition Heat Processing), Vulkan Verlag, Essen, Germany, 2017

[39] Giese, A., Nummerische Untersuchungen zur Bestimmung der Ammenlängen in Drehrohröfen (in German), Ph. D. thesis, Otto-von-Guericke-Universität Magdeburg, Magdeburg, Germany, 2003
[40] Peters, N., *Turbulent Combustion, Cambridge Monographs on Mechanics*, Cambridge University Press, Cambridge, UK, 2000
[41] Hawthorne, W. R., *et al*., Mixing and Combustion in Turbulent Gas Jets, *Symposium on Combustion and Flame and Explosion Phenomena*, *3* (1948), 1, pp. 266-288

Paper submitted: January 9, 2023
Paper revised: February 3, 2023
Paper accepted: February 11, 2023